

Generative Topological Networks

Alona Levy-Jurgenson^{1,2}, Zohar Yakhini^{1,2}

¹Reichman University

²Technion – Israel Institute of Technology

Correspondence: levyalona@gmail.com

Abstract

Generative models have seen significant advancements in recent years, yet often remain challenging and costly to train and use. We introduce *Generative Topological Networks (GTNs)* – a new class of generative models that addresses these shortcomings. GTNs are trained deterministically using a simple supervised learning approach grounded in topology theory. GTNs are fast to train, and require only a single forward pass in a standard feedforward neural network to generate samples. We demonstrate the strengths of GTNs on several datasets, including MNIST, CelebA and the Hands and Palm Images dataset. Finally, the theory behind GTNs offers insights into how to train generative models for improved performance. Code and weights are available at: <https://github.com/alonaj/GTN>

1 Introduction

Deep generative models such as Generative Adversarial Networks (GANs) (Goodfellow et al. 2020), Variational Autoencoders (VAEs) (Kingma and Welling 2013), Energy-Based Models (EBMs) (LeCun et al. 2006; Ngiam et al. 2011), normalizing flows (NFs) (Rezende and Mohamed 2015), and diffusion models (Sohl-Dickstein et al. 2015b), have demonstrated remarkable capabilities for generating samples based on training data distributions (Kang et al. 2023; Ho, Jain, and Abbeel 2020; Ramesh et al. 2021; Ho et al. 2019; Kingma and Dhariwal 2018; Kingma et al. 2016; Reed et al. 2017; Van Den Oord, Vinyals et al. 2017; Ramesh et al. 2021; Onken et al. 2021).

Diffusion models, in particular, have seen great advancements over the last few years in a variety of settings (Ho, Jain, and Abbeel 2020; Luo et al. 2023; Nichol and Dhariwal 2021; Dhariwal and Nichol 2021; Ho et al. 2022; Rombach et al. 2022), and possess several advantages compared to other methods. For example, compared to GANs and VAEs diffusion models have more training stability as they do not suffer from mode collapse like GANs (Zhang, Li, and Yu 2018), or posterior collapse like VAEs (Lucas et al. 2019).

However, diffusion models have several downsides. Most prominent is their inferior time-efficiency during training and sampling when compared to VAEs and GANs. This is because they employ a gradual and stochastic transition from

a Gaussian distribution to the data distribution, performed over multiple time-steps known as the reverse diffusion process. The complexity of this process also makes it challenging to produce interpolations – desirable in the context of continuous data like audio and video. Although recent advancements have made significant steps towards enhancing diffusion models, the complex diffusion process is still a key challenging component (Manduchi et al. 2024).

In this work we introduce a particularly efficient, stable and simple class of generative models – Generative Topological Networks (GTNs). GTNs learn a continuous and invertible mapping between two distributions in a supervised manner that facilitates efficient training and sampling. Specifically, given a training set of samples (e.g. images) and a tractable source distribution (e.g. Gaussian), GTNs learn a function \hat{h} such that, given a y sampled from the source distribution, $\hat{h}(y)$ is a sample representing the training data distribution. GTNs are reminiscent of NFs, which aim to transform one distribution into another using a sequence of invertible and differentiable maps. GTNs, however, are constructed entirely differently, and offer many advantages from both practical and theoretical perspectives.

From a **practical** perspective, GTNs are extremely simple and efficient, requiring a single, vanilla, feedforward architecture trained using standard supervised learning. This means that GTNs avoid the complexities of introducing stochasticity during training which is present in VAE and diffusion; circumvent the intricacies of training more complex architectures such as those employed by diffusion and GANs; are not a likelihood-based approach, as are most generative models; and do not pose constraints on the structure of the neural network, as do NFs. GTNs also operate on latent representations of the data, providing even more enhanced training and sampling efficiency. These advantages manifest in our experiments – realistic samples are obtained at early training epochs, and generating a single image takes around 4 milliseconds on a standard PC and 0.003 milliseconds on a T4 GPU.

From a **theoretical** perspective, GTNs provide guarantees and properties that are desirable in the context of generative models. These include: learnability (via the universal approximation theorem), continuity (for continuous interpolations – Figure 6), bijectivity (for diversity and coverage of the data distribution – Figure 3) and properties that serve

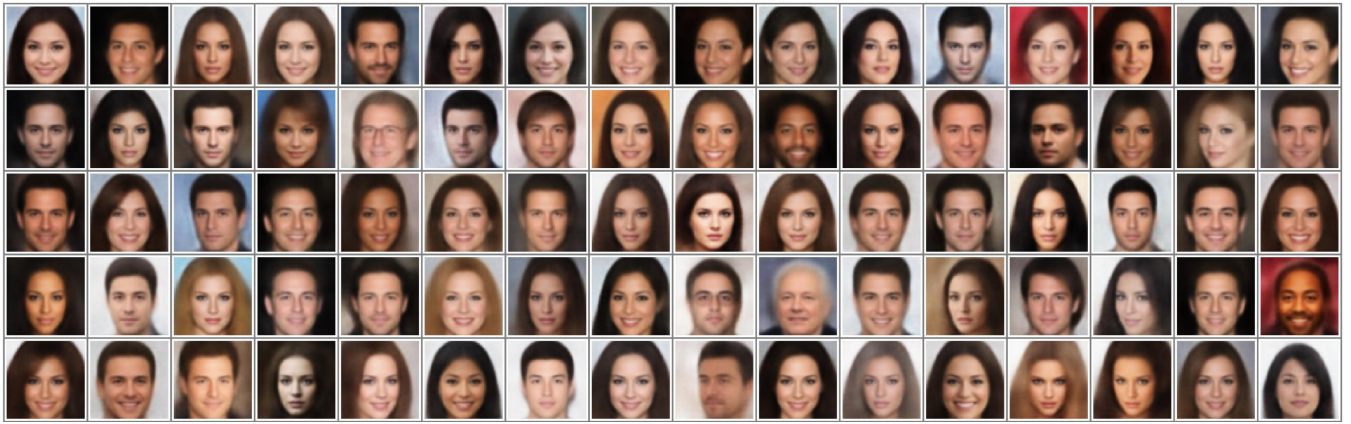


Figure 1: Samples generated by a GTN trained on CelebA 64×64 with a latent dimension of 100.

as guiding topological principles on how to train generative models for better performance (see the Method section and the swiss-roll example).

The remainder of the paper is structured as follows: In the Method section we first develop the theory behind GTNs for the 1-dimensional (1D) case and use it to generate samples from the swiss-roll. We then extend this theory to higher dimensions and use it to generate samples from the multi-variate uniform distribution. In the Experiments section we apply GTNs to real datasets, also including demonstrations of continuous interpolation. We follow with Related Work section and conclude with the Discussion section.

2 Method

We first develop the method in the simple case of a 1D space, and proceed to generalize to higher dimensions.

2.1 1-Dimension

Consider a continuous random variable X with values in \mathbb{R} . We wish to generate samples from X without knowing its distribution. One solution would be to sample from a known and tractable distribution, such as the standard normal distribution, and then to apply a function that maps this sample to a corresponding sample from X . Diffusion models attempt to approximate such a mapping through gradual stochastic manipulations of the standard normal sample back to a sample from X . We will show that, under certain general conditions, such a mapping can be explicitly defined, providing a simple deterministic function which we will denote as h (and which we illustrate in Figure 2). We will show that h is in fact a homeomorphism – it is continuous, invertible and has a continuous inverse (see Definition 2.1). This has significant implications, as we will soon explain.

Defining h . In this section we will define the aforementioned function h that transforms one distribution into another. We will also prove that h , under fairly general conditions, possesses certain properties that are desirable in the context of generative models by proving that it is a homeomorphism (Theorem 2.1). For example, we will see that h is bijective, so that each sample y is mapped precisely to one

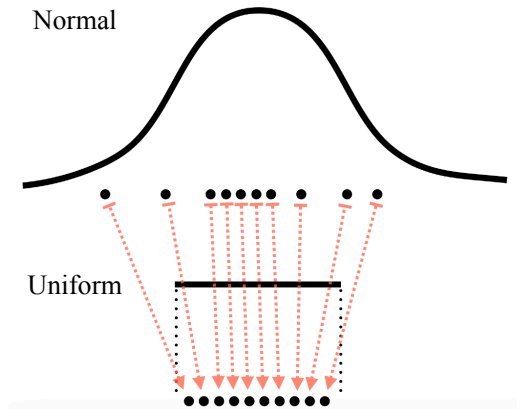


Figure 2: Illustration of the mapping produced by h and of the labeling process for training its approximation \hat{h} , where Y is normally distributed and X is uniformly distributed. A point y from the normal sample is labeled with the unique point x_y from the uniform sample that has the same empirical CDF value as y .

sample $x_y = h(y)$, generating different samples for different y , and guaranteeing that each sample x has a sample y that generates it. We will also discuss other useful consequences of h being a homeomorphism. We begin by defining the term *homeomorphism* in our context and proceed to defining h in Theorem 2.1.

Definition 2.1 (Homeomorphism for \mathbb{R}^n). Let S, T be two subsets of \mathbb{R}^n . A function $h : S \rightarrow T$ is a **homeomorphism** if: (1) h is continuous; (2) h is bijective; (3) h^{-1} is continuous. When such an h exists, then S and T are called **homeomorphic**.

Theorem 2.1 Let X and Y be random variables that have continuous probability density functions (pdfs) f_X, f_Y and supports S_X, S_Y that are open intervals in \mathbb{R} . Denote the corresponding cumulative distribution functions (CDFs) as

F_X and F_Y . Define:

$$\begin{aligned} h : S_Y &\rightarrow S_X \\ h(y) &= F_X|_{S_X}^{-1}(F_Y|_{S_Y}(y)) \end{aligned} \quad (1)$$

Then: (1) h is well-defined; (2) h is a homeomorphism.

Note that the requirement that S_X, S_Y are open intervals can be adapted to a union of open intervals – see Appendix C. The proof of Theorem 2.1 is in Appendix A.

The simple special case of $f_X, f_Y > 0$ in \mathbb{R} illustrates the key ideas of Theorem 2.1. In this case we have that:

$$\begin{aligned} h : \mathbb{R} &\rightarrow \mathbb{R} \\ h(y) &= F_X^{-1}(F_Y(y)) \end{aligned} \quad (2)$$

For simplicity of exposition, we continue with this special case but note that adapting the results to the general case is a matter of technicality. Namely – $f_X, f_Y > 0$ on S_X, S_Y respectively. Combined with S_X and S_Y being open intervals, we conclude that the restricted CDFs $F_X|_{S_X}, F_Y|_{S_Y}$ are continuous and strictly monotonically increasing on S_X, S_Y , which is the main observation needed in order to generalize.

The Significance of h Being a Homeomorphism. The fact that h is a homeomorphism is significant in the context of generative models for several reasons:

1. **Learnability** – Since h being a homeomorphism implies that both h and h^{-1} are continuous real-valued functions over some subset of \mathbb{R} , then by the universal approximation theorem they can be approximated to arbitrary accuracy by a neural network (Hornik, Stinchcombe, and White 1989). *This is demonstrated in Figure 3 (A).*

2. **Coverage and diversity** – The bijectivity of a homeomorphism means that there is a one-to-one and onto correspondence between the supports S_X and S_Y . This means that we can use Y to cover all samples that can be obtained from X and that no two samples in Y will generate the same sample in X . *This is demonstrated in Figure 3 (A) and (B).*

3. **Continuous interpolation** – The fact that h is continuous is significant for purposes of interpolation. For example, given a generative model $g : \mathbb{R} \rightarrow S_X$, two points $y_1, y_2 \in \mathbb{R}$, and the function: $\phi(\lambda) = \lambda y_1 + (1-\lambda)y_2$ (where $\phi : [0, 1] \rightarrow \mathbb{R}$) we would like $(g \circ \phi)(\lambda)$ to be continuous (e.g. for video generation). If g is stochastic, for example, this cannot be guaranteed. However, using h as g , we have that $g \circ \phi$ is continuous as a composition of continuous functions. This provides the desired continuous interpolation between points from X . *This is demonstrated in Figure 6.*

4. **Guiding topological properties** – There are useful properties that are invariant under homeomorphisms (“topological properties”) that can guide us in designing better generative models. For example, one property is that homeomorphic manifolds must have the same dimension. *The use of this property is demonstrated in the upcoming swiss-roll example*, where it will lead us to the conclusion that we are better off generating swiss-roll samples from a 1D standard normal distribution, rather than from a 2D one. Another example for a useful property is in Appendix C.

Learning h Using a Neural Network \hat{h} and Generating Samples with \hat{h} . As explained in the previous subsection, one consequence of h being a homeomorphism is that it can be approximated by a feedforward neural network \hat{h} . If we had known both F_X^{-1} and F_Y then we would be able to easily generate labels for each $y \in Y$: denoting the label of a given $y \in Y$ as x_y , we would set $x_y = h(y)$, meaning:

$$x_y = h(y) = F_X^{-1}(F_Y(y)) \quad (3)$$

Although we do not know F_X, F_Y , we do have access to samples from X and Y which we can use to approximate x_y . From Eq. 3 we see that x_y satisfies $F_X(x_y) = F_Y(y)$, meaning x_y is the unique $x \in X$ that matches the percentile of y . We can use this observation to approximate x_y by replacing F_X and F_Y with the empirical CDFs as follows.

Let $D_X := \{x_1, \dots, x_n\}$ and $D_Y := \{y_1, \dots, y_n\}$ be n observed values of X and Y , respectively. Labels are obtained easily by sorting D_X and D_Y to obtain D_X^{sorted} and D_Y^{sorted} and labeling each $y \in D_Y^{\text{sorted}}$ with the corresponding $x \in D_X^{\text{sorted}}$ (i.e. assuming D_X, D_Y are sorted, y_i is assigned x_i). This is illustrated in Figure 2.

The loss function is the MSE:

$$\frac{1}{n} \sum_{i=1}^n \|\hat{h}(y_i) - x_{y_i}\|^2$$

Generating samples from X is now straightforward – we sample $y \in Y$ and compute $\hat{h}(y)$.

Example: Swiss-Roll. In this example, we will see that samples from the swiss-roll can be easily generated from a 1D normal distribution with visibly near-perfect accuracy (Figure 3 (A)) using a GTN. This would not be as easy using a 2D normal distribution (the approach taken by previous methods such as (Sohl-Dickstein et al. 2015b)), as we will now explain.

The swiss-roll is a 1D manifold in a 2D space \mathbb{R}^2 (generated using a single, 1-dimensional, continuous random variable θ). Being a 1D manifold, it cannot be homeomorphic to the support of a 2D normal distribution (\mathbb{R}^2) since homeomorphic manifolds must have the same dimension. Therefore, there would be no hope of learning a homeomorphism that maps a 2D Gaussian random variable to the swiss-roll. However, the swiss roll *is* homeomorphic to \mathbb{R} – the support of a 1D standard normal distribution. In fact, since θ is a random variable that satisfies the conditions in Theorem 2.1, it is homeomorphic to \mathbb{R} via h , which we can learn using \hat{h} . The fact that there is no hope of learning a homeomorphism in a higher-dimensional space than the intrinsic dimension is also important for NFs, which use a diffeomorphism (a type of homeomorphism) as a generator, and it may also help explain why latent diffusion models have shown improvements over pixel-space diffusion models (Rombach et al. 2022).

To train \hat{h} , we created a dataset of $n = 50,000$ samples from θ , denoted D_X . We sampled n samples from a 1D standard normal distribution to obtain D_Y . We labeled each $y_i \in D_Y$ with its $x_{y_i} \in D_X$ as defined in the previous section. We used a standard feedforward neural network as \hat{h} (4 layers of width 6; details in Appendix Table 1). Figure 3

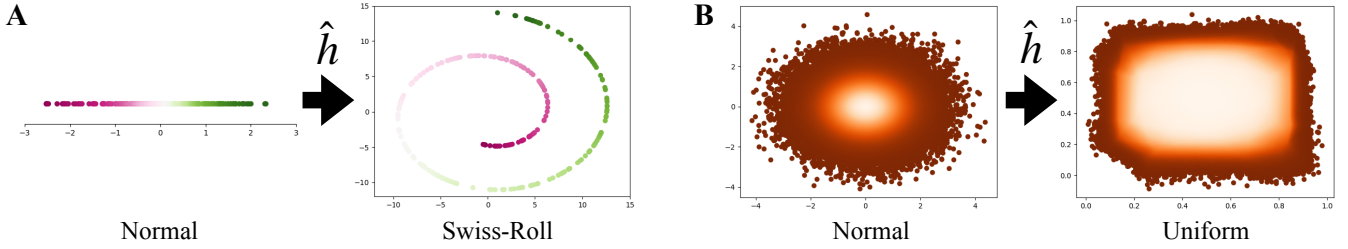


Figure 3: **(A)** Test results for a GTN \hat{h} trained to map from $Y \sim \mathcal{N}(0, 1)$ to the swiss-roll parameter. The color indicates which point in the normal sample was mapped to which point in the swiss-roll. **(B)** Test results for a GTN \hat{h} trained to map from $Y \sim \mathcal{N}(\mathbf{0}, \mathbf{I})$ to $X \sim U((0, 1) \times (0, 1))$. The color is based on the normal sample (left): for each y in the normal sample, $\hat{h}(y)$ has the same color as y so that the figure on the right shows how the normal sample was stretched to a uniform distribution.

(A) shows the result of testing the trained model \hat{h} on a set of new samples y_1, \dots, y_k drawn from $\mathcal{N}(0, 1)$ (each point is obtained by predicting $\hat{\theta}_i := \hat{h}(y_i)$ and applying the formula for the swiss roll to $\hat{\theta}_i$).

For comparison, we refer the reader to Figure 1 (middle) in (Sohl-Dickstein et al. 2015b) where a trained diffusion model was applied to points sampled from a standard 2D normal distribution. The points are gradually and stochastically moved back towards the swiss-roll manifold, but the result contains points that fall outside of this manifold. With \hat{h} , the generated points lie entirely within the data manifold. In fact, this holds true early in the training process, as shown in Appendix Figure 8.

Besides demonstrating that \hat{h} can serve as an accurate generative model, this example also emphasizes an important point – namely, that if we want to learn such a homeomorphism h , we might need to reduce the dimensionality of the data if it is not already in its intrinsic dimension (for the swiss-roll this was 1). This observation will guide us in later sections.

2.2 Higher Dimensions

To generalize to more than one dimension, we reduce to the 1D case by considering lines that pass through the origin. Briefly, we take the random variables obtained by restricting X and Y to each line, and apply the homeomorphism defined for the 1D case to these random variables. We begin with a formal setup that is very similar to the 1D case.

Defining h . Let $X = (X_1, \dots, X_d), Y = (Y_1, \dots, Y_d)$ be multivariate random-variables with continuous joint probability density functions f_X, f_Y , and with supports S_X, S_Y , each of which is a product of d open intervals in \mathbb{R} (see Appendix C to accommodate for other supports). For example, X could be uniformly distributed with support $S_X = (0, 1) \times (0, 1)$ and Y could be normally distributed with support $S_Y = \mathbb{R} \times \mathbb{R}$.

Consider first rotation invariant distributions (e.g., the standard multivariate normal). That is, assume that for every rotation matrix R and every $x \in \mathbb{R}^d$, $f_X(Rx) = f_X(x)$, and similarly for f_Y . For simplicity, also assume that $S_Y, S_X = \mathbb{R}^d$. We can now define the following homeomorphism:

$$h : \mathbb{R}^d \rightarrow \mathbb{R}^d$$

$$h(y) = \begin{cases} h_1(\|y\|) \frac{y}{\|y\|}, & y \neq 0 \\ 0, & y = 0 \end{cases} \quad (4)$$

where $h_1 : (0, \infty) \rightarrow (0, \infty)$ is the 1D homeomorphism applied to the random variables $\|Y\|, \|X\|$.

We prove that this is indeed a homeomorphism in Appendix D. Note that this generalizes the 1D case since for $d = 1$ we get $y \mapsto h_1(y)$. Intuitively, h can be seen as shrinking or stretching y to the unit vector in y 's direction ($y/\|y\|$), and then shrinking or stretching it to reach the $x_y := h(y)$ that has the same ranked distance as y on the line (by multiplying it by $h_1(\|y\|)$). More precisely, h_1 produces x_y 's distance from the origin so that it has the same quantile as y 's distance from the origin (when measured with respect to the random variables obtained by restricting Y, X to the line segment from the origin in y 's direction). Another way of thinking about this is provided in Appendix E.

For more complicated distributions, it may be difficult to explicitly define a similar h since h_1 would depend on the line. Nevertheless, the simpler case above can guide us on how to train a neural network to learn one (as accomplished in Figure 3 (B)).

Learning h . Let D_X and D_Y be observed values from X and Y . Ideally, we would use the 1D labeling scheme on each line that passes through the origin by using h_1 on both sides of the line. In practice, however, the probability that any given line contains points from either D_X or D_Y is negligible. We therefore approximate this labeling approach using cosine-similarity. Specifically, we match y with the x that is closest in terms of both cosine-similarity (so that both y, x_y are as close as possible to being on the same line and in the same direction) and distance from the origin (to approximate $h_1(\|y\|)$). This is formally described in Algorithm 1 and illustrated in Figure 4. To see why Algorithm 1 approximates h , consider a line with an infinite sample from X and Y in both directions from the origin (see Figure 4). The maximal cosine-similarity over all $x \in D_X$ and a y on this line is 1, so the algorithm returns an x_y that is on this line and in y 's direction. Because D_X, D_Y are sorted by distance from the

Algorithm 1: Labeling

Input:

$$D_X = \{x_1, \dots, x_n\}$$

$$D_Y = \{y_1, \dots, y_n\} \text{ sampled from } \mathcal{N}(\mathbf{0}, \mathbf{I})$$

Output: res

```
1:  $res \leftarrow []$ 
2:  $D_X^{\text{sorted}}, D_Y^{\text{sorted}} \leftarrow \text{sort } D_X, D_Y \text{ ascending by } \|\cdot\|_2$ 
3: while  $D_Y^{\text{sorted}} \neq \emptyset$ :
4:    $y \leftarrow D_Y^{\text{sorted}}[0]$ 
5:    $x_y \leftarrow \arg \max_{x \in D_X^{\text{sorted}}} \text{cosine\_sim}(x, y)$ 
6:    $D_Y^{\text{sorted}} \leftarrow D_Y^{\text{sorted}}[1 \dots n]$ 
7:    $D_X^{\text{sorted}} \leftarrow D_X^{\text{sorted}} \setminus \{x_y\}$ 
8:    $res.append((y, x_y))$ 
9: return  $res$ 
```

Algorithm 2: Sampling

Input: \hat{h} trained on res (see Alg. 1)

```
1:  $y \leftarrow \text{sample from } \mathcal{N}(\mathbf{0}, \mathbf{I})$ 
2: return  $\hat{h}(y)$ 
```

origin, ties in cosine-similarity are broken by distance from the origin, so that the first y is matched with the first x , the second y with the second x etc. as in the 1D case, i.e. $\|x_y\|$ approximates $h_1(\|y\|)$. Appendix B gives further intuition.

Using the labeled samples from Algorithm 1, we train \hat{h} – a feedforward neural network – using MSE as the loss function. We then use \hat{h} to generate new X instances just as in the 1D case, formally described in Algorithm 2.

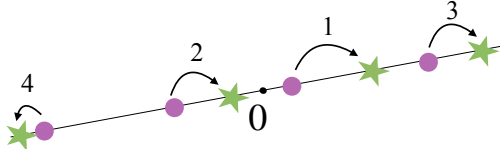


Figure 4: Illustration of Algorithm 1. Numbers reflect the order of matching y (circles) with x_y (stars).

Example: 2-Dimensional Uniform Distribution. Figure 3 (B) shows a sample generated using Algorithm 2 after applying the method to the multivariate uniform distribution $X \sim U(0, 1) \times U(0, 1)$. Specifically, we created D_X by sampling $n = 100,000$ points from X , and created D_Y by sampling the same number of points from $\mathcal{N}(\mathbf{0}, \mathbf{I})$. We then applied Algorithm 1 to D_X, D_Y to generate labeled data. We trained a standard feedforward neural network \hat{h} (6 layers, width 6; details in Appendix Table 1) and used it to generate new samples according to Algorithm 2. The model was trained until convergence on a separately generated validation set with $n = 10,000$. The colors in both images in Figure 3 (B) are based on the distance of the points from the origin in the Gaussian sample (the left image in (B)), so that the image on the right reflects where each point in the Gaus-

sian sample was predicted to 'move' to by \hat{h} .

3 Experiments

In the previous section, we demonstrated how to learn \hat{h} on synthetic data – the swiss-roll and the multivariate uniform distribution. In this section, we will demonstrate how to apply \hat{h} to images.

Setup. In light of the discussion in Section 2.1 on using the intrinsic dimension (ID) of the data, we use autoencoders to represent each dataset in a lower dimensional latent space before training \hat{h} . Each dataset was trained separately (with its own autoencoder and \hat{h}). In all experiments, we use the same vanilla autoencoder architecture adapted to different latent dimensions (the encoder consisted of 2 convolution layers with ReLU activation followed by a fully connected layer). For \hat{h} we use a standard feedforward neural network with the width and depth depending on the data. All architecture and training details for all experiments are in Appendix F.

To train \hat{h} , we set X to be the latent vectors of the training set (the encoded images), and set Y to be the standard multivariate normal distribution of the same dimension as the latent space (e.g., if we used a latent dimension of $d = 100$ in the autoencoder, then Y has dimension 100). Images were generated using Algorithm 2 by computing: $autoencoder.decoder(\hat{h}(r))$ where $r \sim \mathcal{N}(\mathbf{0}, \mathbf{I})$ (generation occurs in the latent space).

Results. We first apply our method to MNIST (LeCun et al. 1998) using a latent dimension of 5. We chose $d = 5$ to allow for comparison with VAE for the same latent dimension (Figure 5(b) in (Kingma and Welling 2013)). Figure 5 shows random sets of generated images for MNIST at several epochs of improvement on the validation set, as well as a sample of random real images for comparison. These results show that the generated samples were already realistic even after one epoch (a similar observation was made for the swiss-roll). Besides the aforementioned comparison to VAE, further comparisons can be made with diffusion (Figure App.1. in (Sohl-Dickstein et al. 2015b)) and a continuous normal flow (CNF) (Figure 3(a) (right) in (Huang and Yeh 2021)). Training was stopped when no improvement in the validation MSE was obtained for 3 epochs.

Next we applied the method to CelebA (Liu et al. 2015) (Figure 1 and Appendix Figures 10-14). Images were center cropped to 148×148 and resized to 64×64 . We tested latent dimensions of $d \in \{10, 25, 50, 100\}$, which are within the range of the typical ID estimated for image datasets (10-50) or close (100) (Pope et al. 2021). We used Inception Score (IS) (Salimans et al. 2016), a common evaluation metric, as the stopping criteria: after every epoch, the GTN generated 200 random images for which the IS was evaluated. We used IS instead of the validation set since the IS continued to improve well beyond the point of plateau on the validation set (for MNIST the IS was irrelevant since the data is grayscale). Training stopped after 300 epochs of no improvement in IS. We also produced the IS for a single random set of 200 real decoded images as a baseline ("real IS"). Plotting the IS by

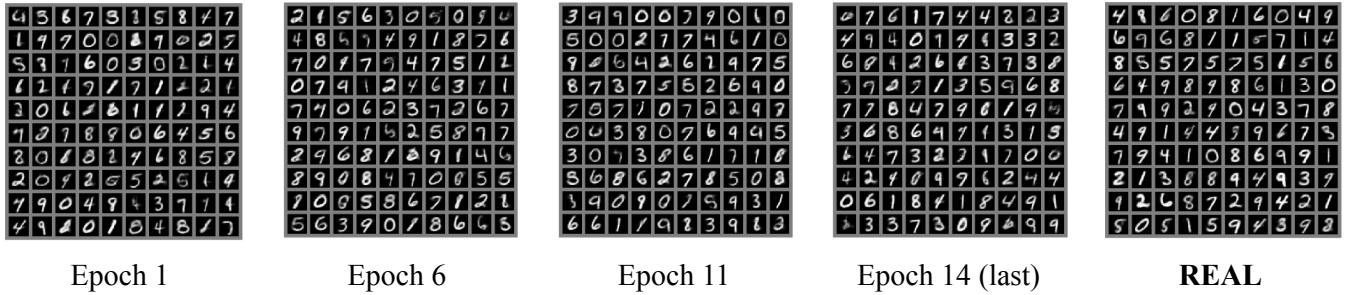


Figure 5: Randomly chosen samples generated by GTN during the training process on MNIST at four points of improvement on the validation set. Each epoch shows 100 images, each of which is the decoded $\hat{h}(r)$ for some random $r \sim \mathcal{N}(\mathbf{0}, \mathbf{I})$. The rightmost grid contains 100 images each of which is the decoded latent vector of a random *real* image.

epoch, alongside the real IS (Appendix Figure 9) shows that the real IS is either achieved ($d = 10, 25$) or nearly achieved ($d = 50, 100$) by the GTN and that the gap between IS and real IS decreases as d decreases. With the final model, we also computed another common evaluation metric – the Fréchet Inception Distance (FID) (Heusel et al. 2017) – between the training set and an equally-sized set of generated images. We observed a similar pattern, namely that FID decreased as d decreased, except for $d = 10$ (Appendix Table 2). Overall, the IS and FID, as well as the difference between IS and real IS, improved as d decreased. Visual inspection of randomly generated images next to real images across all dimensions (Appendix Figures 10-13) confirms these improvements. Namely, as d decreases we see more similarity between generated images and real images as well as improved diversity.

Observing the progress in image generation during training (Appendix Figure 14), we can see that realistic images were already obtained at half the training time (see epoch 276). One epoch took just under 1 minute (50.6 seconds on average) on a single T4 GPU, reflecting 9 hours until the last improvement in IS at epoch 640 and < 4 hours to reach epoch 276. The time to generate 1,000 samples (i.e. to compute: $autoencoder.decoder(\hat{h}(r))$) on a standard PC was 4.07 seconds (reflecting 4.07 *milliseconds per image*) and 0.00367 seconds (reflecting 0.00367 *milliseconds per image*) on a T4 GPU.

We next used the CelebA dataset as well as the Hands and Palm Images (HaP) dataset (Kaggle. 2024) to demonstrate that GTNs indeed provide continuous interpolations. The HaP dataset is a small dataset containing 11,000 images of upward-facing and downward-facing hands. We chose the HaP dataset since generating hands is known to be notoriously difficult for generative models (The New Yorker. 2023; Vox. 2023), let alone interpolating between them. As in CelebA, we trained a GTN for each of the four dimensions, on images resized to 64×64 .

Figure 6 shows interpolations for both CelebA and HaP. For CelebA we used the $d = 100$ model and for HaP we used $d = 50$. The dimensions were chosen after consulting the IS and FID results across all four d values in Appendix Table 2 while preferring a higher dimension ($d \in \{50, 100\}$)

to retain more visual detail (e.g., compare Appendix Figures 10-11 to 12-13): in CelebA $d = 100$ obtained similar results to $d = 50$ and in HaP $d = 50$ obtained better results than $d = 100$. Note that we observe similar trends in HaP as in CelebA: the difference between IS and real IS, as well as the FID decrease with d (Appendix Figure 16 and Table 2).

Figure 6 shows that GTN indeed generates continuous interpolations for both CelebA and HaP. Each row contains generated interpolations between two images (leftmost and rightmost). Specifically, each row contains the results of decoding $\hat{h}(\lambda y_{\text{left}} + (1 - \lambda)y_{\text{right}})$ for 20 linearly spaced $\lambda \in [0, 1]$, where, in CelebA, both y_{left} and y_{right} were sampled from $\mathcal{N}(\mathbf{0}, \mathbf{I})$, and in HaP y_{left} and y_{right} are each the normal label of a real encoded image (from Algorithm 1), chosen so that they have the same orientation.

It is worth noting an interesting observation arising from the HaP dataset. Notice that the generated interpolations in Figure 6 are between hands of the same orientation (downward facing). However, generated interpolations between hands (downward facing) and palms (upward-facing) do not seem as natural (Appendix Figure 15). This is likely because the dataset does not contain in-between positions for the latter (transitions between downward and upward), but it *does* for the former (closed/open fingers to various degrees). This demonstrates that, regardless of methodology, the completeness of the dataset is important for accurate image generation, and particularly for interpolation.

4 Related work

GTNs are related in concept to NFs which seek to map a source distribution into a target distribution using a sequence of bijective transformations. These are typically implemented by a neural network, often in the form of at least tens of neural network blocks (Xu and Campbell 2024) and sometimes more (Xu, Chen, and Campbell 2023). The core of NFs is based on each of these transformations being a diffeomorphism – a specific type of homeomorphism that is more constrained as it is defined between *smooth* manifolds (as opposed to any topological spaces, including any manifolds) and requires that the function and its inverse are *differentiable* (as opposed to just continuous for general homeomorphisms). NFs also require that the log-determinant of

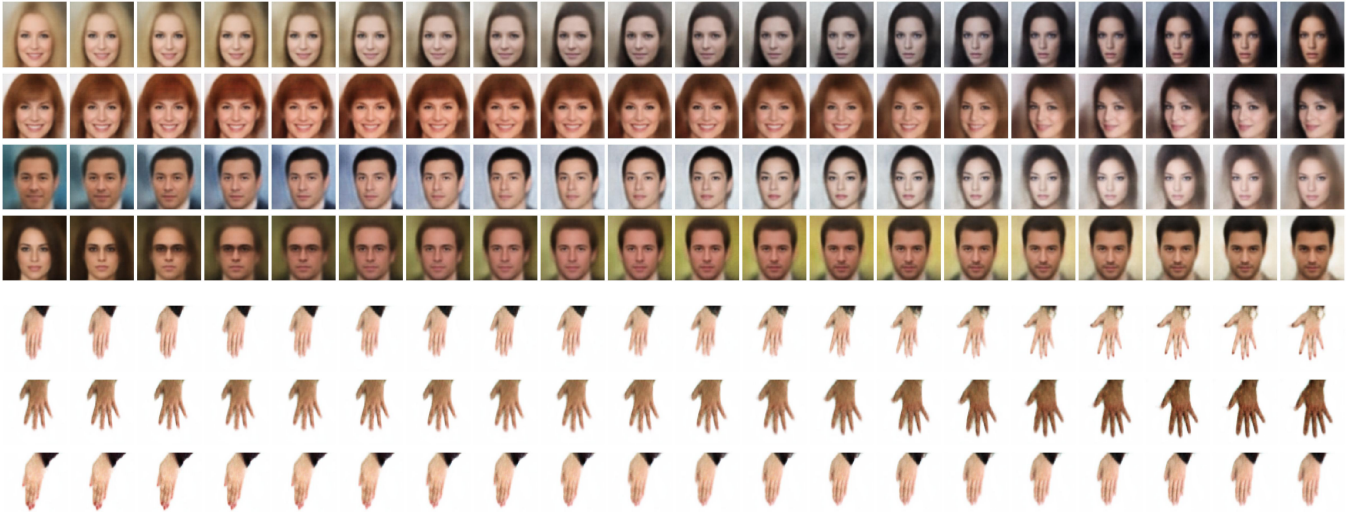


Figure 6: Interpolations generated by a trained GTN for CelebA (top) and the HaP dataset (bottom).

the Jacobian of these transformations is tractable, posing a constraint on the model architecture. GTNs do not pose any limitations on the model architecture. NFs also differ from GTNs in their optimization method since NFs employ a maximum likelihood objective – typically the Kullback-Leibler (KL) divergence while GTNs are trained using MSE. It was observed that optimizing the KL-divergence may be difficult for more complex normalizing flow structures (Xu, Chen, and Campbell 2023). NFs may also suffer from low-quality sample generation (Behrmann et al. 2021), partially because the constraint on the Jacobian, besides limiting the model structure, may also lead to issues such as spurious local minima and numerical instability (Golinski, Lezcano-Casado, and Rainforth 2019).

Continuous normalizing flow (CNF) are a relatively recent type of NFs that were developed to avoid the main constraints posed by NFs – namely the requirements of invertibility and a tractable Jacobian determinant. To avoid these constraints, CNFs use ordinary differential equations (ODEs) to describe the transformations in NFs. While CNFs have provided certain improvements over NFs, they are still time-intensive since they require solving a series of ODEs, equivalent to running a neural network with hundreds of layers (Huang and Yeh 2021). Improving both the speed and performance of CNFs is an active and promising field of research. A comparison between a recent CNF and GTN was suggested in the Experiments section.

5 Discussion

In this work we introduced a new class of generative models – GTNs – that learn a homeomorphism h between the supports of two continuous random variables using samples from both. The samples are used in an efficient algorithm to create a training dataset for the GTN which is trained in a simple supervised approach, with no restrictions on the model architecture. The freedom to use a standard neural network architecture, and the fact that h satisfies the condi-

tions of the universal approximation theorem, lead GTNs to quickly converge towards h , providing an efficient method to generate samples from a target random variable. This was demonstrated experimentally in multiple cases, particularly manifesting in the observation that generated samples reached the data manifold at early epochs and in the total time to convergence. Other positive implications of h being a homeomorphism – namely, coverage and diversity, continuous interpolations and guiding topological properties – were also discussed and demonstrated experimentally.

One downside of our approach is that it relies on the theoretical assumption that the data is represented in its intrinsic dimension. Experimentally, this assumption manifested in different performances and sample quality across different dimensions. This means that dimensionality reduction methods, like the autoencoders used in this work, may be essential for high quality sample generation. Future work, e.g. for generating high-resolution images, may be interested in experimenting with stronger autoencoders as well as additional procedures such as data augmentations, which were not used here. Additionally, the assumptions on the supports of the distributions mean that our method may be ill-suited for discrete distributions, and that datasets may need to be split into separate components for individual training, as explained in Appendix C. The latter case means that larger datasets may be required to ensure that the number of samples per component is sufficiently large. Existing literature on estimating the intrinsic dimension of the data and on the relation between the intrinsic dimension and the required sample complexity (e.g., (Pope et al. 2021)) may be of value in both of these contexts.

References

Behrmann, J.; Vicol, P.; Wang, K.-C.; Grosse, R.; and Jacobsen, J.-H. 2021. Understanding and mitigating exploding inverses in invertible neural networks. In *International Con-*

- ference on Artificial Intelligence and Statistics, 1792–1800. PMLR.
- Dhariwal, P.; and Nichol, A. 2021. Diffusion models beat gans on image synthesis. *Advances in neural information processing systems*, 34: 8780–8794.
- Golinski, A.; Lezcano-Casado, M.; and Rainforth, T. 2019. Improving normalizing flows via better orthogonal parameterizations. In *ICML Workshop on Invertible Neural Networks and Normalizing Flows*.
- Goodfellow, I.; Pouget-Abadie, J.; Mirza, M.; Xu, B.; Warde-Farley, D.; Ozair, S.; Courville, A.; and Bengio, Y. 2020. Generative adversarial networks. *Communications of the ACM*, 63(11): 139–144.
- Heusel, M.; Ramsauer, H.; Unterthiner, T.; Nessler, B.; and Hochreiter, S. 2017. Gans trained by a two time-scale update rule converge to a local nash equilibrium. *Advances in neural information processing systems*, 30.
- Ho, J.; Chen, X.; Srinivas, A.; Duan, Y.; and Abbeel, P. 2019. Flow++: Improving flow-based generative models with variational dequantization and architecture design. In *International conference on machine learning*, 2722–2730. PMLR.
- Ho, J.; Jain, A.; and Abbeel, P. 2020. Denoising diffusion probabilistic models. *Advances in neural information processing systems*, 33: 6840–6851.
- Ho, J.; Salimans, T.; Gritsenko, A.; Chan, W.; Norouzi, M.; and Fleet, D. J. 2022. Video diffusion models. *Advances in Neural Information Processing Systems*, 35: 8633–8646.
- Hornik, K.; Stinchcombe, M.; and White, H. 1989. Multilayer feedforward networks are universal approximators. *Neural networks*, 2(5): 359–366.
- Huang, H.-H.; and Yeh, M.-Y. 2021. Accelerating continuous normalizing flow with trajectory polynomial regularization. In *Proceedings of the AAAI Conference on Artificial Intelligence*, volume 35, 7832–7839.
- Kaggle. 2024. Hands and Palm Images Dataset. <https://www.kaggle.com/datasets/shyambhu/hands-and-palm-images-dataset>. Accessed: 2024-05-15.
- Kang, M.; Zhu, J.-Y.; Zhang, R.; Park, J.; Shechtman, E.; Paris, S.; and Park, T. 2023. Scaling up gans for text-to-image synthesis. In *Proceedings of the IEEE/CVF Conference on Computer Vision and Pattern Recognition*, 10124–10134.
- Kingma, D. P.; and Dhariwal, P. 2018. Glow: Generative flow with invertible 1x1 convolutions. *Advances in neural information processing systems*, 31.
- Kingma, D. P.; Salimans, T.; Jozefowicz, R.; Chen, X.; Sutskever, I.; and Welling, M. 2016. Improved variational inference with inverse autoregressive flow. *Advances in neural information processing systems*, 29.
- Kingma, D. P.; and Welling, M. 2013. Auto-encoding variational bayes. *arXiv preprint arXiv:1312.6114*.
- LeCun, Y.; Bottou, L.; Bengio, Y.; and Haffner, P. 1998. Gradient-based learning applied to document recognition. *Proceedings of the IEEE*, 86(11): 2278–2324.
- LeCun, Y.; Chopra, S.; Hadsell, R.; Ranzato, M.; and Huang, F. 2006. A tutorial on energy-based learning. *Predicting structured data*, 1(0).
- Liu, Z.; Luo, P.; Wang, X.; and Tang, X. 2015. Deep learning face attributes in the wild. In *Proceedings of the IEEE international conference on computer vision*, 3730–3738.
- Lucas, J.; Tucker, G.; Grosse, R.; and Norouzi, M. 2019. Understanding posterior collapse in generative latent variable models.
- Luo, Z.; Chen, D.; Zhang, Y.; Huang, Y.; Wang, L.; Shen, Y.; Zhao, D.; Zhou, J.; and Tan, T. 2023. Videofusion: Decomposed diffusion models for high-quality video generation. In *Proceedings of the IEEE/CVF Conference on Computer Vision and Pattern Recognition*, 10209–10218.
- Manduchi, L.; Pandey, K.; Bamler, R.; Cotterell, R.; Däubener, S.; Fellenz, S.; Fischer, A.; Gärtner, T.; Kirchler, M.; Kloft, M.; et al. 2024. On the Challenges and Opportunities in Generative AI. *arXiv preprint arXiv:2403.00025*.
- Ngiam, J.; Chen, Z.; Koh, P. W.; and Ng, A. Y. 2011. Learning deep energy models. In *Proceedings of the 28th international conference on machine learning (ICML-11)*, 1105–1112.
- Nichol, A. Q.; and Dhariwal, P. 2021. Improved denoising diffusion probabilistic models. In *International conference on machine learning*, 8162–8171. PMLR.
- Onken, D.; Fung, S. W.; Li, X.; and Ruthotto, L. 2021. Ot-flow: Fast and accurate continuous normalizing flows via optimal transport. In *Proceedings of the AAAI Conference on Artificial Intelligence*, volume 35, 9223–9232.
- Pope, P.; Zhu, C.; Abdelkader, A.; Goldblum, M.; and Goldstein, T. 2021. The intrinsic dimension of images and its impact on learning. *arXiv preprint arXiv:2104.08894*.
- Ramesh, A.; Pavlov, M.; Goh, G.; Gray, S.; Voss, C.; Radford, A.; Chen, M.; and Sutskever, I. 2021. Zero-shot text-to-image generation. In *International conference on machine learning*, 8821–8831. Pmlr.
- Reed, S.; Oord, A.; Kalchbrenner, N.; Colmenarejo, S. G.; Wang, Z.; Chen, Y.; Belov, D.; and Freitas, N. 2017. Parallel multiscale autoregressive density estimation. In *International conference on machine learning*, 2912–2921. PMLR.
- Rezende, D.; and Mohamed, S. 2015. Variational inference with normalizing flows. In *International conference on machine learning*, 1530–1538. PMLR.
- Rombach, R.; Blattmann, A.; Lorenz, D.; Esser, P.; and Ommer, B. 2022. High-resolution image synthesis with latent diffusion models. In *Proceedings of the IEEE/CVF conference on computer vision and pattern recognition*, 10684–10695.
- Salimans, T.; Goodfellow, I.; Zaremba, W.; Cheung, V.; Radford, A.; and Chen, X. 2016. Improved techniques for training gans. *Advances in neural information processing systems*, 29.
- Sohl-Dickstein, J.; Weiss, E.; Maheswaranathan, N.; and Ganguli, S. 2015a. Deep unsupervised learning using nonequilibrium thermodynamics. In *International conference on machine learning*, 2256–2265. PMLR.

Sohl-Dickstein, J.; Weiss, E. A.; Maheswaranathan, N.; and Ganguli, S. 2015b. Deep Unsupervised Learning using Nonequilibrium Thermodynamics. *arXiv preprint arXiv:1503.03585*.

The New Yorker. 2023. The Uncanny Failure of A.I. - Generated Hands. <https://www.newyorker.com/culture/rabbit-holes/the-uncanny-failures-of-ai-generated-hands>. Accessed: 2024-05-15.

Van Den Oord, A.; Vinyals, O.; et al. 2017. Neural discrete representation learning. *Advances in neural information processing systems*, 30.

Vox. 2023. Why AI Art Struggles with Hands. <https://www.youtube.com/watch?v=24yjRbBah3w>. Accessed: 2024-05-15.

Xu, Z.; and Campbell, T. 2024. Embracing the chaos: analysis and diagnosis of numerical instability in variational flows. *Advances in Neural Information Processing Systems*, 36.

Xu, Z.; Chen, N.; and Campbell, T. 2023. MixFlows: principled variational inference via mixed flows. In *International Conference on Machine Learning*, 38342–38376. PMLR.

Zhang, Z.; Li, M.; and Yu, J. 2018. On the convergence and mode collapse of GAN. In *SIGGRAPH Asia 2018 Technical Briefs*, 1–4.

Appendix

A

1. h is well-defined: it suffices to show that: (a) $F_X|_{S_X}$ is invertible, and (b) that the image of $F_Y|_{S_Y}$ is in the domain of $F_X|_{S_X}^{-1}$. For (a), observe that $F_X|_{S_X}$ is continuous (the CDF of a continuous random variable is continuous), strictly monotonically increasing (the CDF is strictly monotonically increasing on the support) and onto $(0, 1)$ (by definition of the CDF and the fact that the support is an open interval). As such it is invertible. A symmetric argument can be made for $F_Y|_{S_Y}$, which we will use later to define the inverse of h .

For (b), we know from the proof of (a) that the image of $F_Y|_{S_Y}$ is the domain of $F_X|_{S_X}^{-1}$.

2. h is a homeomorphism since: a. it is continuous as a composition of continuous functions. Indeed, $F_Y|_{S_Y}$ is continuous (the CDF of a continuous random variable is continuous). $F_X|_{S_X}^{-1}$ is also continuous: since $F_X|_{S_X}$ is continuous (as was $F_Y|_{S_Y}$) and bijective (it is invertible, as shown in the first part) we can use the known result that a continuous and bijective function between two open intervals has a continuous inverse (a consequence of the invariance of domain theorem). ; b. it is bijective since the inverse is $F_Y|_{S_Y}^{-1} \circ F_X|_{S_X}$; c. its inverse is continuous: we know from a. and b. that h is continuous and bijective so we can again use the fact that a continuous and bijective function between two open intervals has a continuous inverse.

B

To understand the rationale behind Algorithm 1, imagine four points from each of X and Y lying on the same line, say the x -axis in \mathbb{R}^2 , such that both X and Y have two points on each side of the origin (we assume D_X, D_Y are centralized). See Appendix Figure 7, where circles are from Y and stars are from X . The cosine similarity of each pair of points $\{a, b\}$ with $a \in D_X, b \in D_Y$ is 1 if they are on the same side or -1 if they are on opposite sides. Take the first $y \in D_Y^{\text{sorted}}$ (the closest one to the origin which reflects ~ 50 th percentile since we assumed an equal number of points from Y on both sides). The maximum cosine similarity out of all $x \in D_X^{\text{sorted}}$ is 1, meaning y will be matched with an x on the same side. The fact that D_X is sorted, means that we are using the distance as a tie breaker – out of all $x \in D_X$ that are on the same side as y , the x that is closest to the origin (~ 50 th percentile) will be chosen as x_y . Likewise, the leftmost y will be matched with the leftmost x (both 0th percentile), the rightmost y with the rightmost x (both 100th percentile) etc. Note that if this were in \mathbb{R} , this process coincides with the same labeling process described in the 1D case (illustrated in Figure 2).

C

One example of a topological property is the connectedness property – being a "single piece", like \mathbb{R} , as opposed to "more than one piece", like $(-\infty, -1) \cup (1, \infty)$, is preserved between homeomorphic spaces (so, in particular, these two

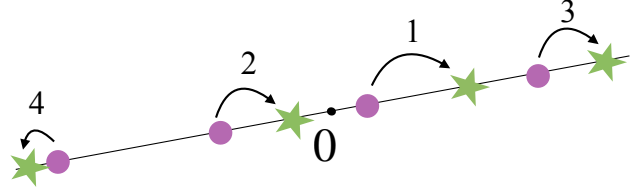


Figure 7: Illustration of Algorithm 1 as described in Appendix B. The numbers reflect the order in which the matching of y with x_y occurs.

are not homeomorphic, but \mathbb{R} is homeomorphic to each of the two intervals, separately). Therefore, if we suspect that our data is composed of separate classes like images of both hands and faces, and we would like to train a GTN as a generative model, we could split our data to its different components (learning a separate h for each). This relates to the conditions of Theorem 2.1 which assume that X 's support is an open interval. For example, if we suspect that our data can be separated into two disjoint uniform distributions, then the theorem doesn't apply. However, it *does* apply to each separate uniformly distributed component.

D

h is injective: equating for two points y_1, y_2 we obtain:

$$h_1(\|y_1\|) \frac{y_1}{\|y_1\|} = h_1(\|y_2\|) \frac{y_2}{\|y_2\|}$$

Applying the norm to both sides yields $h_1(\|y_1\|) = h_1(\|y_2\|)$. Since h_1 is injective, this means that $\|y_1\| = \|y_2\|$. Plugging this into the equality and cancelling out equal terms ($y_1, y_2 \neq 0$) yields $y_1 = y_2$. The function is also onto: since h_1 is onto (it is a homeomorphism) then for any $x \neq 0$ there is a value v in $(0, \infty)$ with $h_1(v) = \|x\|$. Since the support of Y is \mathbb{R}^d there is a y that is on the same line as x from the origin and that satisfies $\|y\| = v$ so that: $x = h_1(\|y\|) \frac{y}{\|y\|}$, meaning that x has a $y \in S_Y$ for which $h(y) = x$.

h is continuous since for $y \neq 0$ it is a composition of continuous functions, and for $y = 0$ we observe that $\lim_{y \rightarrow 0} h_1(\|y\|) \frac{y}{\|y\|} = 0$ ($\frac{y}{\|y\|}$ is the unit vector in the direction of y and $h_1(\|y\|) \rightarrow 0$ as $y \rightarrow 0$ by definition of the CDF).

The inverse is also continuous since a continuous and bijective functions between open subsets of \mathbb{R}^d is continuous (by the invariance of domain theorem).

E

Another way of thinking about this is as follows: assume for simplicity that $f_X, f_Y > 0$ (so that $S_X, S_Y = \mathbb{R}^d$ and therefore $l \cap S_X$ and $l \cap S_Y$ are simply l). Since l is a 1D manifold, X and Y induce 1D random variables X^l and Y^l on the line l , with pdfs f_{X^l}, f_{Y^l} and CDFs F_{X^l}, F_{Y^l} . We can apply Theorem 2.1 to these random variables to obtain a homeomorphism h^l for each line.

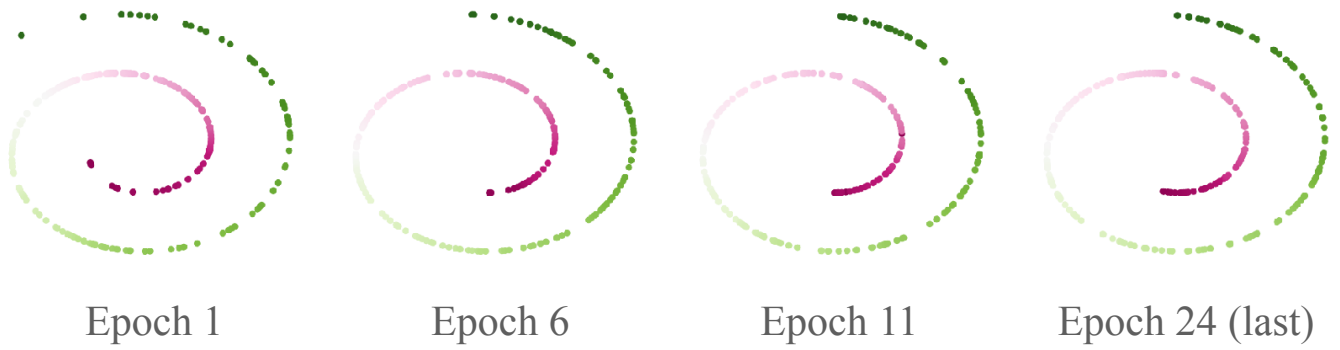


Figure 8: Swiss-roll samples generated by GTN during the training process.

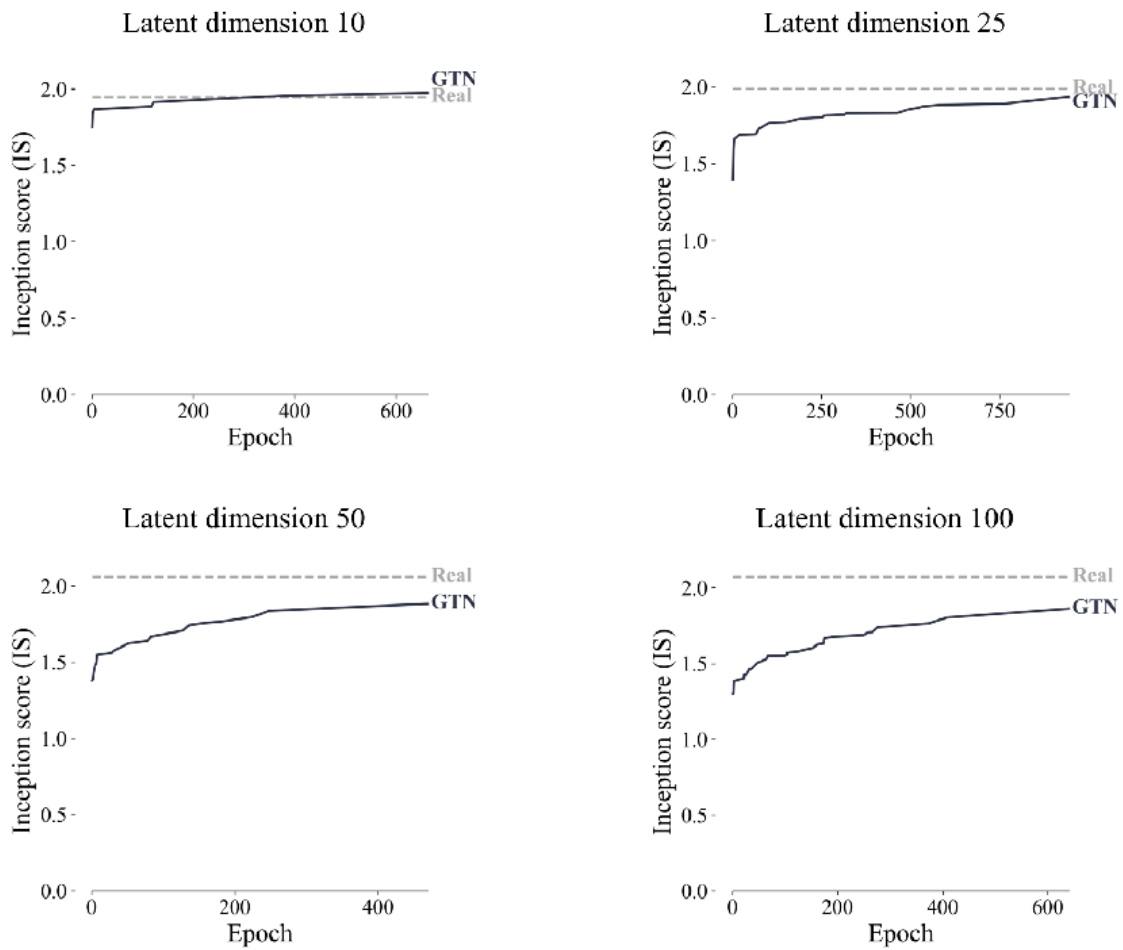


Figure 9: Inception score (IS) vs real IS for CelebA plotted by epoch (at epochs of improvement in the IS). At each epoch, the IS was computed for 200 randomly generated images (decoded latent vectors generated by \hat{h} from random normal vectors, formally: $autoencoder.decoder(\hat{h}(r))$ for $r \sim \mathcal{N}(\mathbf{0}, \mathbf{I})$) (solid black line). Real IS was computed once for a random set of 200 real images (decoded latent vectors of real images) (dashed gray line).

F

The same autoencoder architecture was used for MNIST, CelebA and HaP with only the essential modifications needed to accommodate to the different input channels (1 for MNIST and 3 for CelebA and HaP) and the different latent dimensions. The architecture consisted of a decoder with two 2d convolutional layers followed by ReLU activation: the first convolutional layer had 64 output channels, kernel size 4, stride 2 and padding 1. The second convolutional layer consisted of 128 output channels, kernel size 4, stride 2 and padding 1. The two convolutional layers were followed by a linear layer with the number of output features set to the desired latent dimension d . The output activation was tanh. In the decoder we used a mirror architecture of one linear layer, with the number of input features being d , and two 2d transposed convolution layers. The code for all architectures is also available in our repository. To train the autoencoders we used: a batch size of 200 for CelebA and HaP, and 128 for MNIST; learning rate $1e-4$ for CelebA and HaP and $1e-3$ for MNIST; a weight decay of $1e-5$ was used in all three. We tested the two learning rates $1e-3$ and $1e-4$. No further optimizations were made for the autoencoder hyperparameters.

CelebA images were center-cropped to 148×148 and resized to 64×64 . HaP images were resized to 64×64 .

We did not use any data augmentations during the training process.

Final architecture specifications for \hat{h} appear in Appendix Table 1. We ran a hyperparameter search for CelebA and HaP. Initially, we ran several settings for CelebA using a small number of epochs (roughly 100-300) for latent dimension 200 prior to consulting the literature on the intrinsic dimension of image data. We tried learning rates of $1e-3, 1e-4, 1e-5, 5e-5$ for various width and depth settings. Specifically, for CelebA we tested widths of 500, 1000, 1200, 1300, 1500 and depths of 10, 17, 20, 25, 27. For HaP we kept the depth at 25 after observing this obtained best results for CelebA and tested depths of 2000, 3000 as well after identifying that HaP benefited from higher width settings.

The architectures were compared based on their IS score at each epoch. The architecture with the highest IS score was kept. These architectures are the ones described in Appendix Table 1.

We used the best settings, shown in Appendix Table 1, regardless of the dimension d . We did not perform architecture optimizations per dimension. Such optimizations may provide further improvements in efficiency and/or generative quality.

Each experiment was run on 1 NVIDIA T4 GPU with 8 vCPU + 52 GB memory, 500GB SSD. Specifically, we used the "Deep Learning VM" by Google Click to Deploy in the Google Cloud Marketplace (image: pytorch-1-13-cu113-v20230925-debian-10-py37), modified to the aforementioned specifications.



Figure 12: Generated vs real samples for latent dimension $d = 50$. (A) Random generated samples – each image is the decoded $\hat{h}(r)$ for some random $r \sim \mathcal{N}(\mathbf{0}, \mathbf{I})$. (B) Random real decoded images – each image is the decoded latent vector of a random real image.



Figure 13: Generated vs real samples for latent dimension $d = 100$. (A) Random generated samples – each image is the decoded $\hat{h}(r)$ for some random $r \sim \mathcal{N}(\mathbf{0}, \mathbf{I})$. (B) Random real decoded images – each image is the decoded latent vector of a random real image.



Figure 14: Randomly chosen samples generated by a GTN during the training process on CelebA with latent dimension 100 at several epochs of improvement in the IS score, and randomly chosen real images (bottom-right grid). Specifically, each epoch shows 200 images, each of which is the decoded $\hat{h}(r)$ for some random $r \sim \mathcal{N}(\mathbf{0}, \mathbf{I})$. The bottom right grid shows 200 images each of which is the decoded latent vector of a random real image. Training until epoch 640 took approximately 9 hours on a single T4 GPU, with similar-quality images obtained in less than 4 hours of training at epoch 276.



Figure 15: Interpolations between a hand (downward facing) and a palm (upward facing).

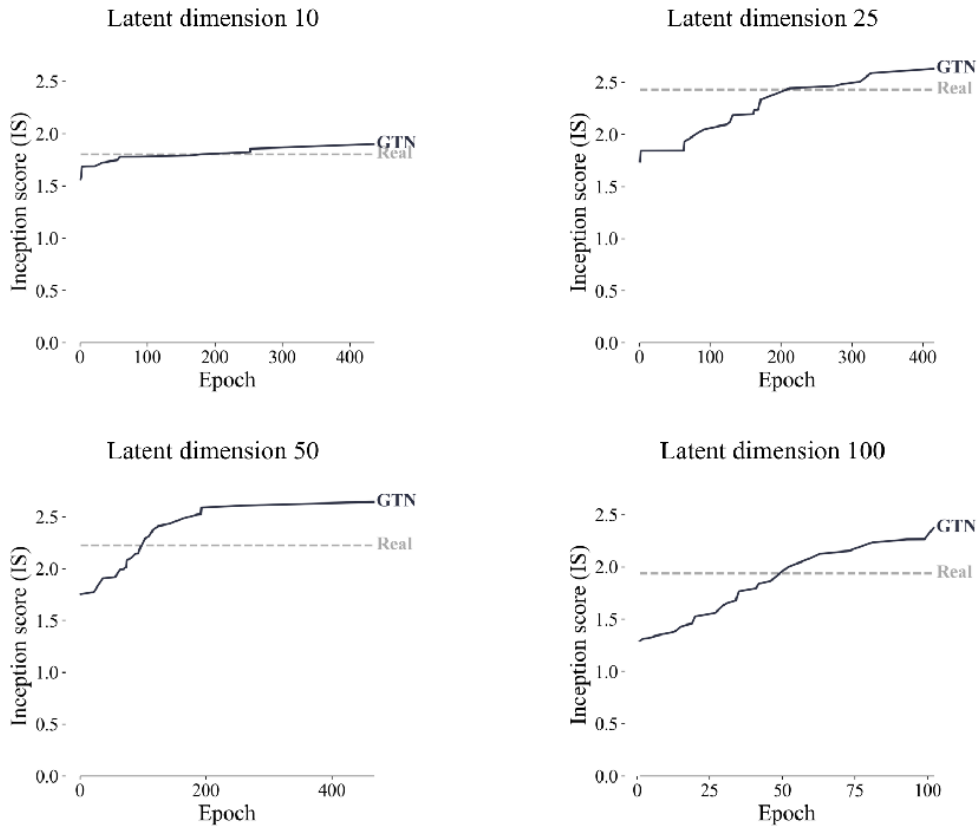


Figure 16: Inception score (IS) vs real IS for HaP plotted by epoch (at epochs of improvement in IS). At each epoch, IS was computed for 200 randomly generated images (decoded latent vectors generated by \hat{h} from random normal vectors), formally: $autoencoder.decoder(\hat{h}(r))$ for $r \sim \mathcal{N}(\mathbf{0}, \mathbf{I})$ (solid black line). Real IS was computed once for a random set of 200 real images (decoded latent vectors of real images) (dashed gray line).

	No. Hidden Layers	Width	Activation	Batch Norm.	Learning Rate	Weight Decay	Optimizer	Batch Size
Swiss-Roll	4	6	LeakyReLU(0.5)	No	$1e^{-3}$	No	Adam	250
Uniform	6	6	LeakyReLU(0.5)	No	$1e^{-3}$	No	Adam	250
MNIST	7	50	LeakyReLU(0.5)	Yes	$1e^{-3}$	No	Adam	128
CelebA	26	1,200	LeakyReLU(0.5)	Yes	$5e^{-5}$	No	Adam	200
HaP	26	3,000	LeakyReLU(0.5)	Yes	$5e^{-5}$	No	Adam	200

Table 1: Architecture specifications for \hat{h} for the different datasets. The architecture was kept the same between the different dimensions where relevant (CelebA, HaP).

	CelebA			HaP		
	IS \uparrow	IS real	FID \downarrow	IS \uparrow	IS real	FID \downarrow
$d = 10$	1.97	1.95	36.66	1.90	1.80	81.50
$d = 25$	1.93	1.99	32.11	2.63	2.43	88.85
$d = 50$	1.88	2.06	33.84	2.64	2.22	88.34
$d = 100$	1.86	2.07	36.43	2.37	1.94	124.62

Table 2: Results per dataset and latent dimension. Inception Score (IS) is the best IS attained for the given dimension and dataset for a random set of 200 generated images. IS real is the IS attained by a set of 200 random real images (decoded latent vectors of real encoded images). Fréchet Inception Distance (FID) is computed for the same model that attained the reported IS using all training images and a same-sized set of randomly generated images.